Yi et al. *Microsystems & Nanoengineering* (2025)11:130
https://doi.org/10.1038/s41378-025-00987-3

Microsystems & Nanoengineering
www.nature.com/micronano

ARTICLE Open Access

A battery-free wireless sensor for encrypted signal transmission via Maxwell's displacement current

Jixin Yi[1], Shuzhe Liu[1], Zhenqiu Gao[1], Shaokuan Wu[1], Haifeng Ji[1], Jiaxun Hou[1], Guyu Jiang[1], Xuhui Sun[1] and Zhen Wen[1]✉

Abstract

Traditional wireless sensors still face challenges such as high power consumption and bulky signal transmission modules. In this work, we report a battery-free sensor via Maxwell's displacement current for encrypted signal transmission. The sensor employs an instantaneous discharge triboelectric nanogenerator (ID-TENG) featuring a dual-contact electrode structure. It enables rapid charge transfer and instantaneous current generation (~6 ms per cycle) and then high-frequency electromagnetic wave generation. The instantaneous discharge mechanism reduces the generated voltage to 100 V while maintaining μA-level current output, addressing critical safety concerns. By integrating a resistor–inductor–capacitor (RLC) equivalent circuit, the sensor achieves precise amplitude and frequency modulation of wireless signals. A series of inductors (0–50 μH) is used to achieve wide frequency-domain regulation (3.91–16.97 MHz), and capacitor parallel regulation (0–50 pF) to achieve accurate regulation in the narrow frequency domain (1.95–2.63 MHz). The sensor illustrates 22 m of wireless transmission distance and sustained stability over 16,000 cycles. By pre-setting the frequency sequence of the signal as a password, the specific password transmits the specific information to realize the encryption of the wireless signal transmission. Finally, it is demonstrated to be used as a smart wireless keyboard, an interactive dance carpet and an encrypted vehicle control system with passivity, adaptability, scalability, and resistance to signal interference.

Introduction

Currently, the rapid advancement of the Internet of Things (IoT) has spurred unprecedented demand for wireless sensing systems in diverse applications[1,2], ranging from smart homes[3,4], healthcare to industrial automation and human–computer interaction[5–10]. As nerve endings of the IoT[11], sensors have attracted a great deal of attention[12]. A critical challenge in this domain lies in developing energy-efficient[13], cost-effective[14], and maintenance-free sensors capable of transmitting signals over long distances without reliance on external power sources[15]. Traditional wired sensors often depend on batteries or complex energy-harvesting systems, which introduce limitations such as finite lifespan[16], environmental concerns, complex wiring, high maintenance costs and restricted applications[17], further hindering their large-scale application and diffusion. To overcome these bottlenecks, sensors are currently moving toward being portable[18], battery-free and wireless[19]. In this trend of change, wireless signal transmission technology plays a crucial role[20,21]. With the sharp increase in the number of distributed sensor nodes, how to achieve wireless signal transmission efficiently and stably has become a key issue[22]. To address the challenges of wireless sensing, sensors are often combined with wireless communication modules[23], such as Wi-Fi, Bluetooth, near-field communication (NFC)[24], LC resonance or narrow-band Internet of Things (NB-IoT)[25]. However, the energy consumption, signal interference and transmission distance of these wireless sensing technologies still pose challenges to some extent.

Triboelectric nanogenerators (TENGs) have emerged as an energy conversion technology through the coupling effect of triboelectrification and electrostatic induction[26–29]. Owing to the simple and versatile structural

Correspondence: Zhen Wen (wenzhen2011@suda.edu.cn)
[1]Institute of Functional Nano and Soft Materials (FUNSOM), Jiangsu Key Laboratory for Carbon-Based Functional Materials & Devices, Soochow University, Suzhou 215123, People's Republic of China
These authors contributed equally: Jixin Yi, Shuzhe Liu

design and wide variety of materials[30], TENGs are uniquely lightweight and self-powered[31], with great advantages for the development of energy-efficient[32], economical[33,34], maintenance-free and battery-free wireless distributed sensors[35]. Recently, a variety of promising TENG-based wireless sensing solutions have been proposed[36,37]. In 2021, Zi et al. firstly proposed a paradigm shift in a fully self-powered long-distance wireless sensing solution enabled by a discharge-induced displacement current[38]. Its related applications only depend on adjusting the structural parameters to modulate the amplitude. In 2022, Luo et al. reported an electric-field-resonance-based wireless triboelectric nanogenerator[39], the output of the TENG can be transmitted wirelessly by integrating the TENG with a capacitive coupler. But its transmission distance and application scenarios are limited. In 2024, our group proposed a battery-free wireless tactile sensor for multimodal force perception that couples the triboelectric and capacitive effects for normal and shear force fusion sensing[40]. It uses coil-to-coil LC resonance to couple the voltage output to the LC circuit and obtain a fixed eigenfrequency signal for wireless sensing. However, this method has a low signal output and a short wireless communication distance.

In this work, we designed a battery-free wireless sensor to transmit electromagnetic waves and receive them via a coil and a back-end circuit to access the IoT. It consists of individual instantaneous discharge wireless passive triboelectric sensors (ID-TENG) with a dual-contact electrode structure. The rapid charge transfer and instantaneous current generation of ID-TENG facilitate the emission of high-frequency EM waves for wireless signal transmission. This mechanism not only enhances the signal generation speed but also amplifies the output characteristics. The incorporation of a resistor–inductor–capacitor (RLC) equivalent circuit enables precise modulation of wireless signals. We realized wireless signal modulation of amplitude and frequency by adjusting the circuit configuration and establishing a remote passive wireless sensing platform. To demonstrate the versatility of the wireless sensing platform, we implemented a smart wireless keyboard, an interactive dance carpet and an encrypted vehicle control system. The sensor achieves long-distance wireless transmission with a low voltage output that reduces safety hazards, substantiating its immense potential for applications across smart homes, leisure and entertainment, vehicle control and human–machine interaction.

Results and discussion

The schematic of the wireless sensor for encrypted signal transmission is illustrated in Fig. 1a. The wireless sensing system consists of an ID-TENG to excite EM waves and a coil to receive the wireless signal to access the IoT. The detailed structural diagram of the ID-TENG, which consists of a contact-separate body part as well as a dual-contact electrode, is shown in Fig. 1b. Specifically, two acrylic sheets were used as the top and bottom substrates and fixed by four springs, and a piece of foam was attached to the center of the bottom acrylic substrate as a buffer between the bottom electrode and the acrylic substrate for soft contact and to ensure that the top electrode could make contact with the bottom contact electrode. Copper foils were used as electrodes attached to the foam and top acrylic substrates. Furthermore, nylon and Ecoflex were used as positive and negative tribolayers, respectively. The preparation process of the Ecoflex film is shown in Fig. S1. The surface of the Ecoflex film was modified via the plasma debonding method to create nanostructures for larger contact areas. SEM images are shown in Fig. S2, we can see that nanostructures are formed only on plasma-treated samples. Figure 1c illustrates the principle of electromagnetic wave release through the dual-contact electrode. During the operation of the sensor, the top electrode of the TENG moves back and forth in the dual-contact electrode structure. The triboelectric charges generated on the nylon and Ecoflex surfaces accumulate on the electrodes due to electrostatic induction. When the top electrode instantaneously contacts the dual-contact electrode, the accumulated charges undergo rapid transfer through the external circuit, generating a transient current with a steep rise time. This rapid current variation induces a time-varying magnetic field, which, according to Maxwell's equations, is accompanied by a time-varying electric field (displacement current), collectively forming propagating electromagnetic waves. The dual-contact electrode structure effectively acts as a transient dipole radiator, where the abrupt charge redistribution during discharge creates a time-varying dipole moment. This dipole oscillation, coupled with the RLC circuit's resonance, enhances the coupling of high-frequency components into free space, enabling efficient EM wave emission without requiring a traditional antenna. This sensor is characterized by instantaneous triggering, wireless transmission, signal modulation, and power management. Photographs of the ID-TENG fabricated from the top view and front view are shown in Fig. 1d, e, with an overall size of 40 × 40 × 20 mm (length × width × height) (the fabrication process is described in detail in the Experimental section). Figure 1f shows the two basic wireless signals generated by this sensor, where the frequency-domain signal is obtained from the time-domain signal through the fast Fourier transform (FFT). Figure S3a, b show enlarged views of these two wireless signals detected at a distance of 10 cm from the coil, both of which are composed of high-frequency peaks and resonance peaks generated by the coil. The schematic of the measurement setup is

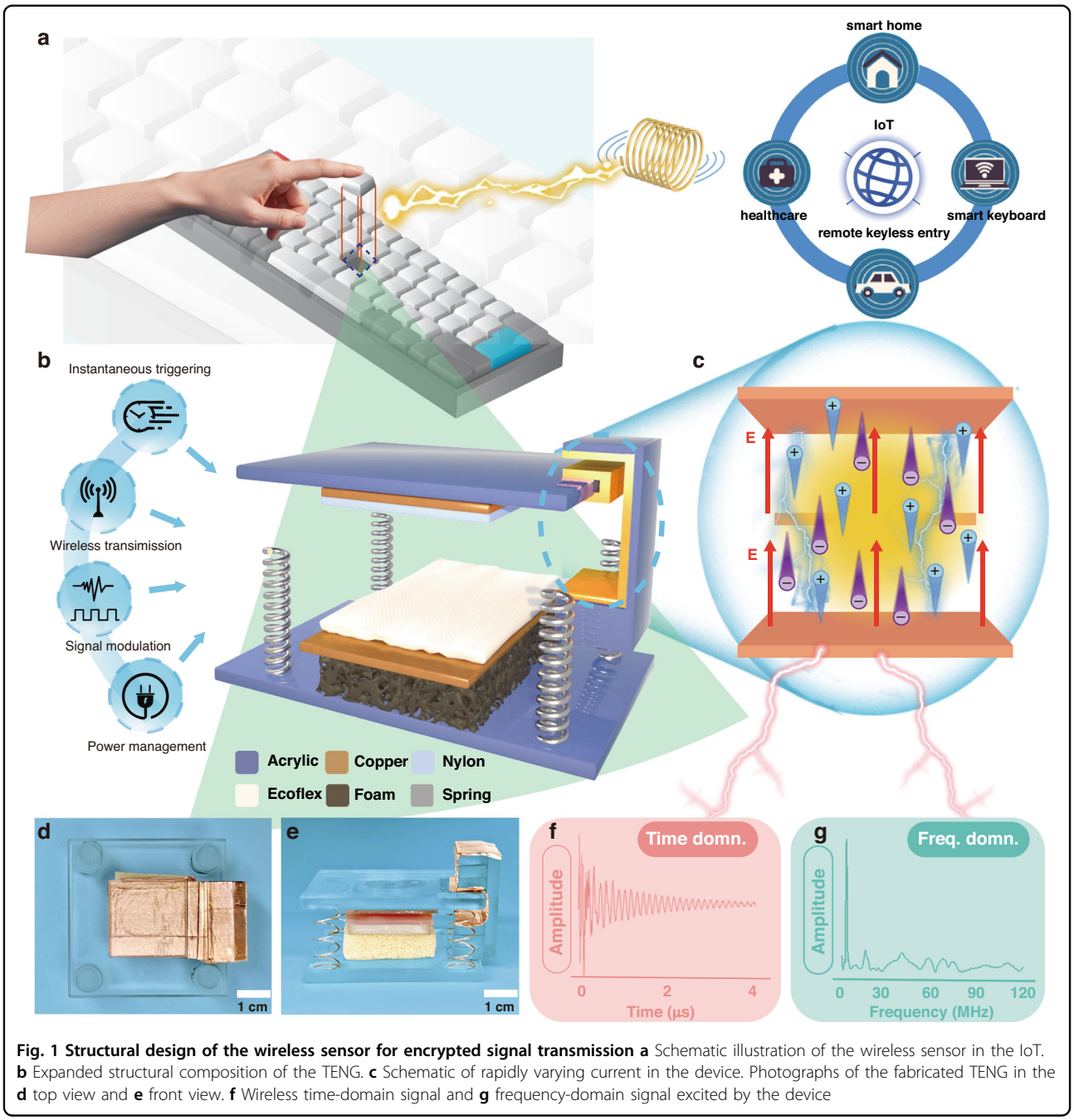

Fig. 1 Structural design of the wireless sensor for encrypted signal transmission a Schematic illustration of the wireless sensor in the IoT. **b** Expanded structural composition of the TENG. **c** Schematic of rapidly varying current in the device. Photographs of the fabricated TENG in the **d** top view and **e** front view. **f** Wireless time-domain signal and **g** frequency-domain signal excited by the device

shown in Fig. S3c. Moreover, we verified the omnidirectionality of the wireless signal, and the signal strength detected in each direction was almost the same, as shown in Fig. S4.

Figure 2a shows the working mechanism (i–vi) of the ID-TENG within one cycle. On the basis of the coupling effect of triboelectrification and electrostatic induction, equal amounts of negative and positive charges are generated on the surfaces of the triboelectric materials in physical contact, as shown in the initial stage i. Here, we consider that nylon and Ecoflex have already been charged with positive and negative charges, respectively, before this. In Stage II, the positive and negative tribolayers are in contact, and the foam is not compressed. Since the top electrode does not come into contact with the dual-contact electrode structure, no charge transfer occurs, and no current is generated in the circuit at this time. When the top electrode contacts the lower contact electrode in Stage III, the foam is extremely compressed, and the mechanical switch is turned on. At this moment,

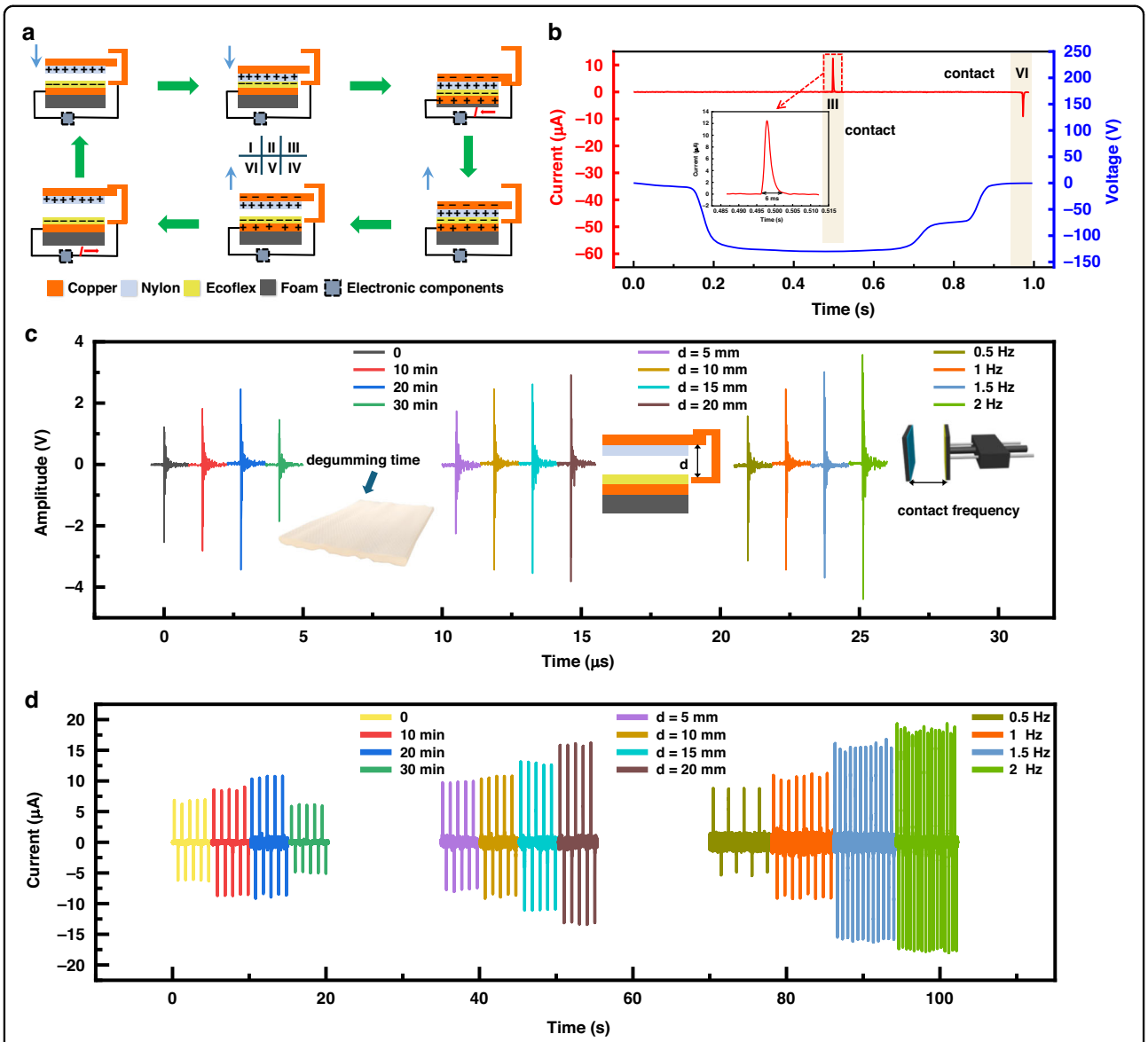

Fig. 2 Working mechanism and output performance of the ID-TENG a Schematic illustration of the working principle of the ID-TENG. **b** Teardown diagram of the short-circuit current I_{sc} and open-circuit voltage V_{oc} in one cycle of the ID-TENG. **c** Wireless time-domain signal and **d** I_{sc} of the ID-TENG under different working conditions

the charges accumulated at both ends are instantaneously transferred, generating a clockwise current in the circuit. According to Maxwell's displacement current equation:

$$J = \varepsilon_0 \frac{\partial E}{\partial t} + \frac{\partial P}{\partial t} \quad (1)$$

where J is the displacement current, ε_0 is the permittivity in vacuum, and E and P are the electric field and polarized electric field, respectively. The first term $\varepsilon_0 \partial E/\partial t$ plays a critical role in the generation of electromagnetic waves. In our system, the dual-contact electrode enables rapid charge transfer during instantaneous discharge, creating a transient current that drives oscillations in the integrated RLC circuit. The RLC circuit (with tunable inductance L_s and capacitance C_p) amplifies high-frequency components of the transient current and couples them to the dual-contact electrodes, which act as a compact dipole radiator. The abrupt charge redistribution across the electrodes generates a time-varying dipole moment, and the RLC resonance enhances the radiation efficiency at specific frequencies. This combined mechanism (displacement

current-driven transient fields and resonant circuit amplification) enables effective EM wave emission without a traditional antenna. In stages iv and v, the foam rebounds, and the two tribolayers gradually separate. However, the mechanical switch in the circuit is disconnected, and no charge transfer occurs. When the top electrode touches the bottom contact electrode in stage vi, the charges between the top and bottom electrodes are transferred through the external circuit, the potential difference is neutralized, and a counterclockwise current is generated. Figure 2b shows an enlarged view of the real-time short-circuit current I_{sc} and open-circuit voltage V_{oc} of a single cycle of the ID-TENG. When the top electrode contacts the contact electrode structure in stages iii and vi, a current is generated in the circuit. The peak of a single current signal is shown in the inset, and the process from the generation to the disappearance of the current lasts only 6 ms. When comparing it with the contact-separation TENG (CS-TENG) shown in Fig. S5, according to the real-time electrical signals and the enlarged current diagram presented in Fig. S5, we can observe that during the approach and separation process between the tribolayers in stages ii and iv of the CS-TENG, a current signal of 2.5 μA is generated. This process lasts as long as 30 ms, which is five times greater than that of the ID-TENG. However, their voltage outputs are essentially the same. Figures S6 and S7 simulate the potential change processes of the ID-TENG and the CS-TENG, respectively, during one cycle, corroborating the results of the same voltage output. According to the wireless signals of the ID-TENG and the CS-TENG received by the oscilloscope, as shown in Fig. S8, the rapidly changing current generated under the working mechanism of the ID-TENG leads to the generation of wireless signals. The performance of the ID-TENG under various operating conditions was experimentally evaluated. We systematically investigated the effects of the degumming time of the Ecoflex surface, the movement distance of the top electrode, and the contact frequency of the device on the performance of the ID-TENG, as shown in Fig. 2c. With increasing degumming time of the Ecoflex surface, the amplitude first increases but then decreases. Among them, at 20 min, the peak-to-peak voltage $U_{p\text{-}p}$ can reach a maximum value of 6.2 V. Figure S9 shows the surface morphology and etching depth of the Ecoflex characterized by a 3D microscope. The reason for this change may be that plasma degumming can increase the surface roughness of the Ecoflex film, increase the contact area of the tribolayer, and increase the output. However, when the degumming time is 30 min, the etching depth reaches 10 μm, which is close to the thickness of the Ecoflex film itself (12 μm), resulting in damage to the film and causing the output to decline. As d varies from 5 mm to 20 mm, the $U_{p\text{-}p}$ of the ID-TENG gradually increases from 4 V to 6.74 V. Meanwhile, the $U_{p\text{-}p}$ of the wireless time-domain signal increases from 4.72 V to 7.98 V as the contact frequency increases from 0.5 Hz to 2 Hz. As shown in Fig. 2d, the variation law of the short-circuit current of the ID-TENG is consistent with that of $U_{p\text{-}p}$. Figures S10 and S11 present comparative analyses of the measurement results of the open-circuit voltage V_{oc} and the transferred charge Q_c under different movement distances d and contact frequencies f. Remarkably, V_{oc} and Q_c remained unaffected and exhibited saturation at 100 V and 40 nC, respectively, irrespective of d ranging from 5–20 mm and f ranging from 0.5–2 Hz. Figure S12 shows the frequency-domain wireless signals of the ID-TENG under these working conditions. We can observe that the frequency remains constant at 2 Hz. Therefore, different working conditions and the device itself have no influence on the frequency. In addition, the measured matching impedance is approximately 1 GΩ, and the power density can reach 16 mW (Fig. S13). Figure S14 shows the electrical performance and wireless signal stability of ID-TENG. After nearly 16000 cycles of operation, I_{sc} still remains at 14 μA, and the waveform of the wireless time-domain signal remains almost unchanged, demonstrating its excellent stability. Therefore, a device with a degumming time of 20 min and a top-electrode movement distance of 20 mm was used in subsequent tests.

Figure 3 shows the modulation of the amplitude and frequency of the wireless signal of the ID-TENG. To characterize the wireless output signal of the ID-TENG, we constructed a resistor–inductor–capacitor (RLC) equivalent circuit system (Fig. 3a). The TENG is equivalent to a voltage source V_{TENG}, a capacitor C_{TENG}, and a mechanical switch. When the top electrode touches the contact electrode, the switch is closed, and at this time, the wireless signal is released. In the remaining stages, the switch is in the open state. L_0, R_0, L_s, and C_p represent the inductance, resistance of the system itself, the additional inductance in series, and the additional capacitance in parallel, respectively, where L_s and C_p are added to modulate the wireless signal output from the circuit system. Figure 3b and S16a show time-domain diagrams with different additional inductances in series. The amplitude of the sinusoidal oscillation increases with increasing additional inductance, reaches the maximum value at 22 μH, and then gradually decreases. Moreover, in the frequency-domain diagram, as the additional inductance increases, the peak of the base frequency (the strongest and lowest frequency) of the received signal gradually shifts to the left (Fig. 3c and S16b) and overlaps with the LC resonance peak at 22 μH, as shown in the inset. This indicates that the receiver reaches a perfect resonance state, and the amplitude of the sinusoidal oscillation is the largest at this time.

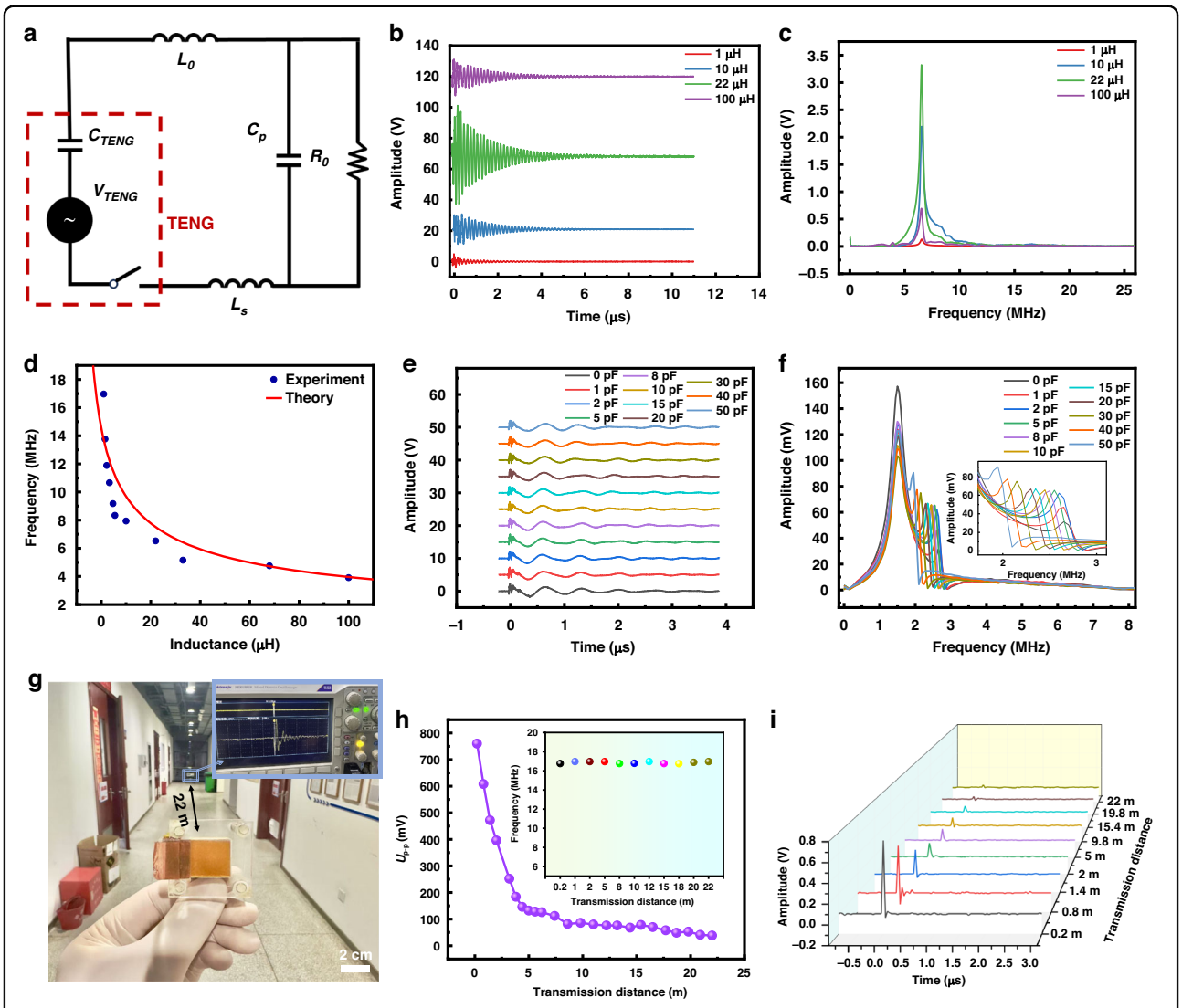

Fig. 3 Wireless sensing performance of the ID-TENG a Electrical model of the ID-TENG with series L_s and parallel C_p. **b** Time-domain diagram and **c** frequency-domain diagram of the wireless signals with different series inductances. **d** Relationship between the base frequency and series inductors. **e** Time-domain diagram and **f** frequency-domain diagram of the wireless signals with different numbers of parallel capacitances. **g** Wireless signal can be detected at a distance of more than 22 m. **h** Relationship between the peak-to-peak voltage of the received signal and the distance between the transmitter and receiver. The inset is a frequency-domain diagram of the wireless signals at different transmission distances. **i** 3D time-domain diagram of the wireless signals at different transmission distances

The base frequency f of the equivalent circuit of the ID-TENG can be calculated as

$$f = \frac{1}{2\pi\sqrt{(L_s + L_0)C_0}} \tag{2}$$

where the system inductance L_0 is measured to be 7.62 μH and the system capacitance C_0 is measured to be 13.56 pF.

According to Eq. (2), the relationship between the theoretical and experimental points of the additional series inductance L_s and the base frequency f of the ID-TENG is plotted in Fig. 3d. The base frequency varies from 16.97 to 3.92 MHz, which is highly consistent with the experimental results. The reason for the slight deviation of some data may be interference from spatial conductors in the experimental environment. These results confirm the equivalent circuit model of the ID-TENG. By changing the values of different parallel capacitances C_p, the time-domain signals when C_p changes from 0 to 50 pF are shown in Fig. 3e. As shown in the time-domain waveforms, with increasing parallel capacitance, the oscillation period increases, and the amplitude decreases. Figure 3f shows the changes in the frequency-domain signals during the change in the parallel capacitance. The resonance

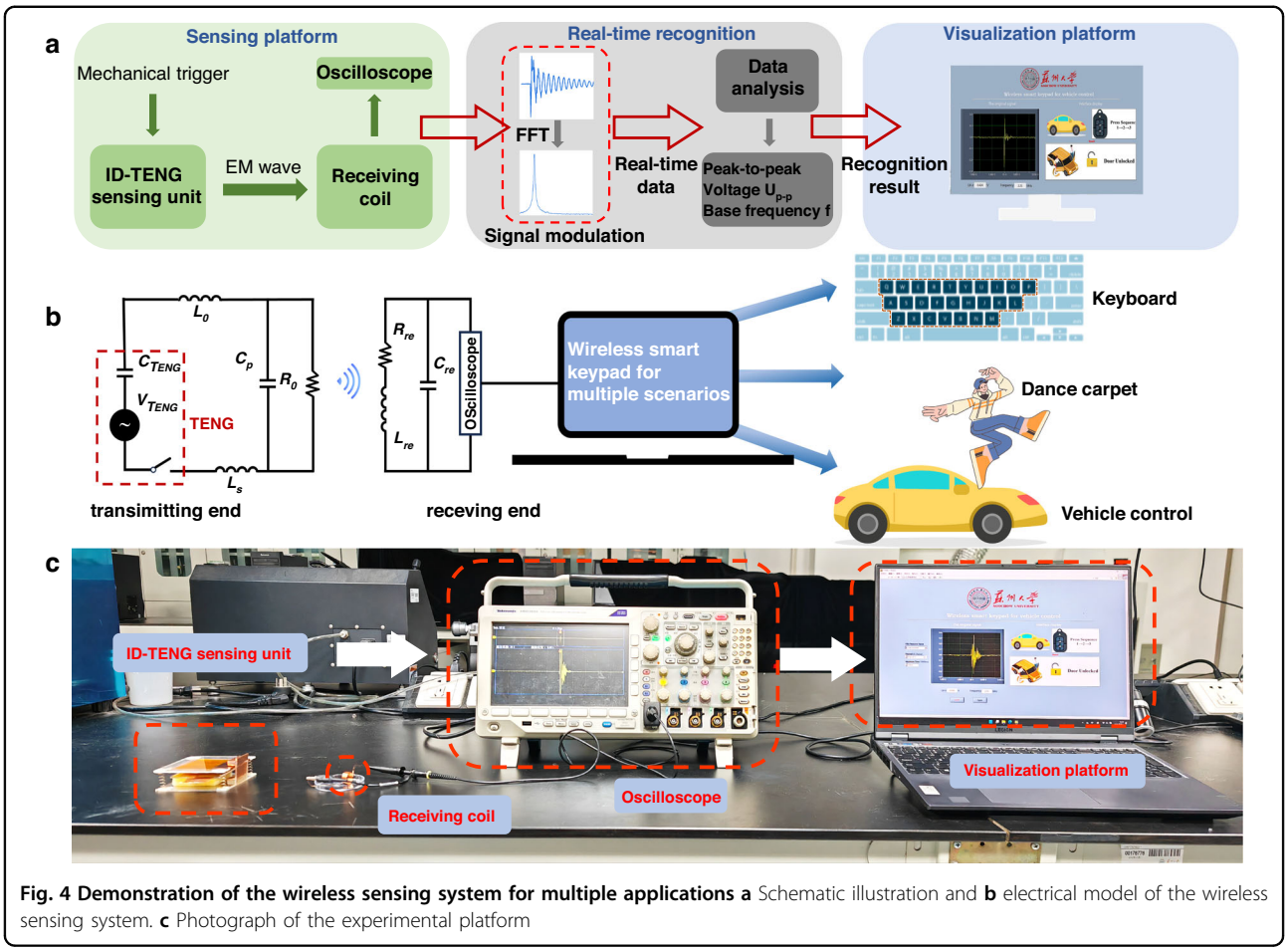

Fig. 4 Demonstration of the wireless sensing system for multiple applications a Schematic illustration and **b** electrical model of the wireless sensing system. **c** Photograph of the experimental platform

frequency remains constant, and the base frequency f gradually decreases from 2.65 MHz to 1.95 MHz. Furthermore, the ID-TENG has the advantage of a long transmission distance. We demonstrated that the EM signal can be detected by a receiver with a long transmission distance of over 22 m, as shown in Fig. 3g. Figure 3h shows the specific relationship between the peak-to-peak voltage $U_{p\text{-}p}$ and the wireless transmission distance. The inset shows the frequency-domain diagram of these signals, which demonstrates that the base frequency f remains constant at different transmission distances. The three-dimensional time-domain signals at various distances are presented in Fig. 3i. The amplitude decreases from 800 mV detected at 0.2 m to 38.4 mV detected at 22 m.

Owing to its battery-free, wireless, high sensitivity, instantaneous triggering, low-cost, and good stability, the ID-TENG can be widely used in signal sensing and transmission without any additional power supplies. Therefore, we developed a wireless sensing system suitable for multiple scenarios in which wireless EM waves are processed and processed data are displayed in real-time. Figure 4a shows the flow chart from EM signal generation, reception, and modulation to computer interface display recognition. The wireless EM wave signals are transmitted by pressing the smart keypad with the finger and are received by the receiving end, composed of the coil and the oscilloscope. By using a USB cable, the signal received by the oscilloscope can be transmitted to the computer in real-time. The computer converted the time-domain signal into a frequency-domain signal via fast Fourier transform (FFT) and visualized the results. The visual interface was programmed in LabVIEW 2018. The electrical model of the wireless sensing system for multiple scenarios is shown in Fig. 4b. It can be used for a wireless keyboard, dance carpet, and vehicle control. Figure 4c shows the actual test scenario of the wireless sensing platform. The signal waveform and recognition results can be displayed on the visualization platform in real-time.

Based on the wireless sensing system, we present three battery-free wireless sensing applications of the ID-TENG below. First, we designed a smart wireless keyboard for letter identification with 26 gadgets integrated into it. Figure S15 shows a schematic diagram of the wireless sensing system for letter identification. A photograph of

the smart wireless keyboard is shown in Fig. S16. Its overall size is 23 × 9 × 5 cm (length × width × height), which is essentially equivalent to a commercial keyboard. Inside, 26 small devices are integrated by staggered stacking, as shown in Fig. S17. By adjusting the circuit configuration of the ID-TENG, such as the value of the series inductor, the frequency band can be changed to distinguish the signal from each key. Figure 5a shows the frequency-domain signals of eight smart keypads and their matching letters. The letter "T" corresponds to 16.9 MHz, the letter "E" corresponds to 13.8 MHz, the letter "N" corresponds to 11.9 MHz, the letter "G" corresponds to 10.7 MHz, the letter "S" corresponds to 7.9 MHz, the letter "U" corresponds to 6.5 MHz, and the letter "D" corresponds to 4.75 MHz. The letter "A" corresponds to 3.9 MHz. Their 3D time-domain diagram is shown in Fig. 5b. Figure S20 demonstrates the frequency-domain signals and base frequency corresponding to the other 18 letters. Figure 5c shows a demonstration interface of a wireless smart keyboard for letter identification to visualize the typing effects of different letters. In the interface, all the collected data, including the time-domain signal, the peak voltage $U_{p\text{-}p}$, the base frequency f derived from the FFT, and the recognized letters, can be displayed simultaneously in real-time (Movie S1). The different signals accurately correspond to different letters, which indicates the ability of this wireless sensing system to perform multiple key, continuous and wireless sensing signals. In addition, we design ID-TENGs of different sizes to suit different application scenarios. Figure S18 is a single sensing unit with dimensions of 85 × 85 × 20 mm (length × width × height). Six such sensing units are placed under the dance carpet to form a wireless smart dance carpet. The actual test scene is shown in Fig. S19. When the animation on the LabVIEW interface reaches the top, the tester presses the corresponding direction keypad to stimulate the wireless electromagnetic wave signal. At this time, the word "perfect" pops up on the interface, which means that the transmitted signal matches the programmed signal successfully. The frequency-domain diagram corresponding to each direction and the base frequency f are shown in Fig. 5d. "Left", "upper left", "upper", "lower", "upper right", and "right" correspond to 1.85, 2.05, 2.15, 2.3, 2.45, and 2.6 MHz, respectively (Movie S2). Figure 5e shows the LabVIEW interface of the smart wireless keypad for the dance carpet. This application proves that the wireless sensing system has the ability for human-computer interaction and variable size. Finally, we designed an encrypted wireless smart keypad for vehicle control. The design process and the physical diagram are shown in S20. The 12 cm by 4 cm capsule car key accommodates three ID-TENG sensing units measuring 36 mm × 20 mm × 15 mm (length × width × height). Figure 5f shows the control principle of the wireless smart car key and the corresponding frequency-domain diagram of the three keys. Keys "1", "2", and "3" correspond to base frequencies of 9.1, 8.3, and 2.35 MHz, respectively. We applied the encryption function to the wireless smart car key, and the order of pressing the three keys was different from the transmission of instructions to the car. When we press keys "1", "2" and "3" in sequence, the door will unlock; the door will lock when you press "1", "3", "2"; and "3" "2" "1" will be pressed to close the window (Movie S3). This encryption function ensures that only the owner of the car can remotely control the car by triggering the keys sequentially. The LabVIEW interface of wireless smart keypads for vehicle control is shown in Fig. 5g. This demonstrates the portable, encrypted capabilities of the wireless sensing system.

Conclusion

In summary, a low-cost, zero-power consumption, no-crosstalk wireless sensor for encrypted signal transmission based on the ID-TENG suitable for multiple application scenarios is reported. The sensor has a simple structure and preparation process, instantaneous triggering, no power supply, strong anti-interference ability and is suitable for a variety of application scenarios. Compared with the traditional contact-separation TENG, the ID-TENG produces a large instantaneous current and varies rapidly, enabling wireless signal transmission with a low open-circuit voltage. The wireless signal generation relies on two synergistic mechanisms: (1) the dual-contact electrode structure enables instantaneous discharge and rapid charge transfer, producing a transient current with steep temporal variation (~6 ms); and (2) the integrated RLC resonant circuit amplifies and modulates the high-frequency components of this current, creating time-varying electromagnetic fields that radiate efficiently into free space. By adjusting external circuits, such as series inductance and parallel capacitance, we achieve precise control over the emitted signal's frequency and amplitude, enabling long-distance wireless transmission (22 m) and encrypted communication. On this basis, the application display of an intelligent wireless keyboard, dance carpet and encrypted car remote control key is realized through the LabVIEW interface program. Overall, we provide a promising solution for battery-free wireless multi-functional long-distance signal-modulable wireless sensing, which can be applied to smart homes, leisure and entertainment, vehicle control and human–computer interaction.

Experimental section

Fabrication and modification of the Ecoflex film

First, Components A and B of Ecoflex 00–30 were mixed at a mass ratio of 1:1, then evenly stirred and poured onto the acrylic sheet and placed in a spin coater

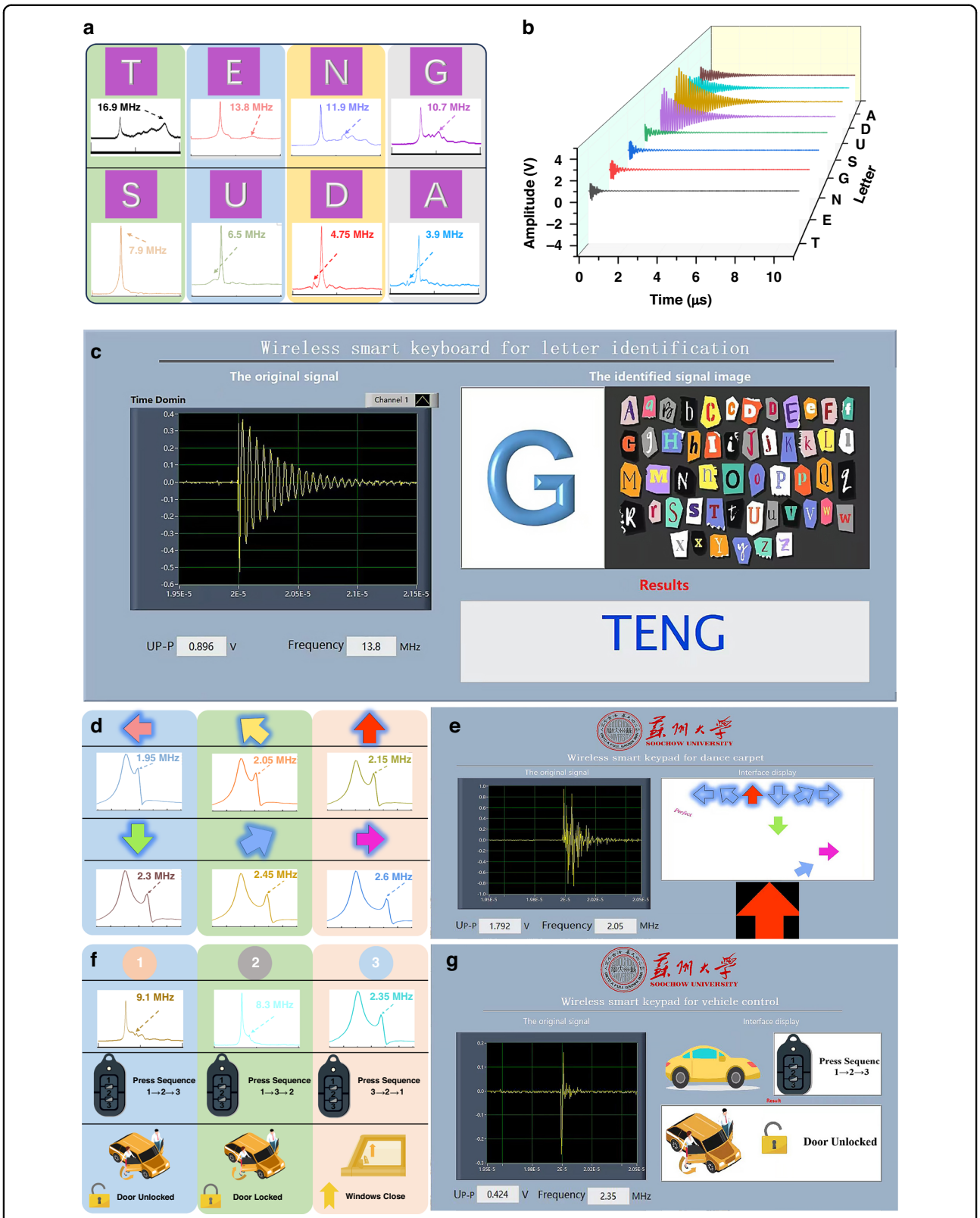

Fig. 5 Demonstration of the wireless sensing system for three different applications a Frequency-domain diagram and **b** 3D time-domain diagram of the wireless signals of individual letter keys. **c** Visualization interface of the wireless smart keyboard. **d** Frequency-domain diagram corresponding to each direction. **e** Visualization interface of the wireless smart dance carpet. **f** Frequency-domain diagram corresponding to each key and working mechanism of the wireless smart car key. **g** Visualization interface of the wireless smart car key

(KW-4BC) running at 300 rpm for 6 s. Then, the acrylic sheet was placed in a vacuum drying oven for 10 min, removed and cured at room temperature for 10 h to obtain a 12 μm-thick Ecoflex film. Second, the Ecoflex film was placed in a plasma glue remover (IoN 40) chamber and etched with 300 W O_2 plasma for 10, 20 or 30 min. After that, the treated samples were cleaned with DI water and dried in a vacuum drying oven before use.

Fabrication of the TENG

The TENG consists of a contact-separate TENG component and a dual-contact electrode component. For the contact-separate TENG component, two 3 mm-thick acrylic sheets were cut by a laser cutting machine (Huitian 4060) into top and bottom substrates with dimensions of 40 × 40 mm. A 20 × 20 mm foam layer (10 mm thick) was attached to the center of the bottom acrylic substrate. Copper foil of the same size was attached to the foam layer and the top acrylic substrate. Next, the Ecoflex film (12 μm thick) and nylon film (100 μm thick) of the same size as above were attached to the surfaces of the top and bottom tribolayers. Moreover, the top copper foil was extended outward and wrapped around the upper edge of the top acrylic substrate as a mechanical contact. Finally, four springs (6 × 6 × 15 mm) were fixed between two acrylic substrates. For the dual-contact electrode component, a bow-shaped acrylic sheet (20 × 10 × 25 mm) was attached to the bottom acrylic substrate. The copper foil was attached to the inside of the bow-shaped acrylic sheet as a mechanical contact with the contact-separate TENG component.

Experimental measurements

A 3D microscope (DCM8) was used to characterize the surface morphology and etching depth of the Ecoflex film. For the basic output performance of the TENG, a linear motor (MTS201) was used to apply external mechanical stimulation to the TENG. A programmable electrometer (Keithley 6514) was used to test the wired electrical output signal. An LCR meter (TH2840B model) with a driving frequency of 1 MHz was used to measure the capacitance and inductance. An oscilloscope (MDO 3024) was used to test the wireless output signals of the circuit. The electrical properties of the materials were simulated via COMSOL Multiphysics software. The measured signals and displayed images are visualized in a high-speed data acquisition system under LabVIEW 2016.

Acknowledgements

This work was supported by the National Key R&D Program of China (No. 2023YFB3208100), the National Natural Science Foundation of China (No. 62174115, No. U21A20147), the Natural Science Foundation of Jiangsu Province of China (No. BK20240152), the Natural Science Foundation of the Jiangsu Higher Education Institutions of China (No. 24KJA430011), the Collaborative Innovation Center of Suzhou Nano Science & Technology, the 111 Project, and the Joint International Research Laboratory of Carbon-Based Functional Materials and Devices.

Author contributions

J.Y., S.L., and Z.W. conceived and oversaw the project. J.Y., S.L., and Z.G. fabricated the devices and performed electrical tests. S.W., H.J., and J.H. operated material characterizations. J.H., G.J., and G.L. programmed codes for image processing. J.Y. and S.L. analyzed the results and wrote the manuscript. X.S. and Z.W. offered the resources for experimental.

Conflict of interest

The authors declare no competing interests.

Supplementary information The online version contains supplementary material available at https://doi.org/10.1038/s41378-025-00987-3.

Received: 7 March 2025 Revised: 19 April 2025 Accepted: 24 May 2025
Published online: 30 June 2025

References

1. Haight, R., Haensch, W. & Friedman, D. J. S. Solar-powering the Internet of Things. *Science* **353**, 124–125 (2016).
2. Zhang, Q. et al. Human body IoT systems based on the triboelectrification effect: energy harvesting, sensing, interfacing and communication. *Energy Environ. Sci.* **15**, 3688–3721 (2022).
3. Shi, Q. et al. Deep learning enabled smart mats as a scalable floor monitoring system. *Nat. Commun.* **11**, 4609 (2020).
4. Choi, H. W. et al. Smart textile lighting/display system with multifunctional fibre devices for large scale smart home and IoT applications. *Nat. Commun.* **13**, 814 (2022).
5. Qin, X. et al. Wearable electrodriven switch actively delivers macromolecular drugs to fundus in non-invasive and controllable manners. *Nat. Commun.* **16**, 33 (2025).
6. Hussain, F. et al. A framework for malicious traffic detection in IoT healthcare environment. *Sensors* **21**, 3025 (2021).
7. Li, D. et al. Touch IoT enabled by wireless self-sensing and haptic-reproducing electronic skin. *Sci. Adv.* **8**, eade2450 (2022).
8. Liu, Y. et al. Electronic skin as wireless human-machine interfaces for robotic VR. *Sci. Adv.* **8**, eabl6700 (2022).
9. Zhu, H. et al. Frequency-encoded eye tracking smart contact lens for human–machine interaction. *Nat. Commun.* **15**, 3588 (2024).
10. Jung, Y. H. et al. A wireless haptic interface for programmable patterns of touch across large areas of the skin. *Nat. Electron.* **5**, 374–385 (2022).
11. Kim, W. G. et al. Triboelectric nanogenerator: structure, mechanism, and applications. *Acs Nano* **15**, 258–287 (2021).
12. Wang, H., Fu, J., Wang, J., Su, L. & Zi, Y. Tribophotonics: an emerging self-powered wireless solution toward smart city. *Nano Energy* **97**, 107196 (2022).
13. Geng, S. et al. An artificial neuromuscular system for bimodal human–machine interaction. *Adv. Funct. Mater.* **33**, 2302345 (2023).
14. Kim, S. Y. et al. Sustainable manufacturing of sensors onto soft systems using self-coagulating conductive Pickering emulsions. *Sci. Rob.* **5**, eaay3604 (2020).
15. Toor, A. et al. Stencil-printed Lithium-ion micro batteries for IoT applications. *Nano Energy* **82**, 105666 (2021).
16. Niu, H. et al. Micropyramid array bimodal electronic skin for intelligent material and surface shape perception based on capacitive sensing. *Adv. Sci.* **11**, 2305528 (2023).
17. Boutry, C. M. et al. A hierarchically patterned, bioinspired e-skin able to detect the direction of applied pressure for robotics. *Sci. Rob.* **3**, eaau6914 (2018).
18. Wang, H. et al. A flexible lightweight self-powered wireless metal detector enabled by triboelectric discharge effect. *Device* **1**, 100127 (2023).
19. Liu, T.-L. et al. Battery-free, tuning circuit–inspired wireless sensor systems for detection of multiple biomarkers in bodily fluids. *Sci. Adv.* **8**, eabo7049 (2022).
20. Wilson, P. F. & Ma, M. T. Fields radiated by electrostatic discharges. *IEEE Trans. Electromagn. Compat.* **33**, 10–18 (1991).
21. Kim, Y. et al. Chip-less wireless electronic skins by remote epitaxial freestanding compound semiconductors. *Science* **377**, 859–864 (2022).

22. Huang, Y. et al. A skin-integrated multimodal haptic interface for immersive tactile feedback. *Nat. Electron.* **6**, 1020–1031 (2023).
23. Hajiaghajani, A. et al. Textile-integrated metamaterials for near-field multibody area networks. *Nat. Electron.* **4**, 808–817 (2021).
24. Lin, R. et al. Wireless battery-free body sensor networks using near-field-enabled clothing. *Nat. Commun.* **11**, 444 (2020).
25. Yair, M. et al. N-BaIoT—network-based detection of iot botnet attacks using deep autoencoders. *IEEE Pervasive Comput.* **17**, 12–22 (2018).
26. Fan, F., Tian, Z. & Wang, Z. Flexible triboelectric generator. *Nano Energy* **1**, 328–334 (2012).
27. Wang, Z. L. On Maxwell's displacement current for energy and sensors: the origin of nanogenerators. *Mater. Today* **20**, 74–82 (2017).
28. Huo, Z. et al. Triboelectrification induced self-powered microbial disinfection using nanowire-enhanced localized electric field. *Nat. Commun.* **12**, 3693 (2021).
29. Ryu, H. et al. Self-rechargeable cardiac pacemaker system with triboelectric nanogenerators. *Nat. Commun.* **12**, 4374 (2021).
30. Zhao, H. et al. Underwater wireless communication via TENG-generated Maxwell's displacement current. *Nat. Commun.* **13**, 3325 (2022).
31. Xie, L. et al. Ultrasensitive wearable pressure sensors with stress-concentrated tip-array design for long-term bimodal identification. *Adv. Mater.* **36**, 2406235 (2024).
32. He, S. et al. Biomimetic bimodal haptic perception using triboelectric effect. *Sci. Adv.* **10**, eabo6793 (2024).
33. Wang, H. et al. Direct muscle stimulation using diode-amplified triboelectric nanogenerators(TENGs). *Nano Energy* **63**, 103844 (2019).
34. Wen, F. et al. Advances in chemical sensing technology for enabling the next-generation self-sustainable integrated wearable system in the IoT era. *Nano Energy* **78**, 105155 (2020).
35. Liu, F. et al. Self-powered wireless body area network for multi-joint movements monitoring based on contact-separation direct current triboelectric nanogenerators. *InfoMat* **5**, e12428 (2023).
36. Si, J. et al. Long-distance multifunctional wireless sensing platform for identifying and ranging. *Nano Energy* **109**, 108267 (2023).
37. Wang, H. et al. A general self-powered wireless sensing solution based on triboelectric-discharge effect. *Nano Energy* **105**, 107982 (2023).
38. Wang, H. et al. A paradigm shift fully self-powered long-distance wireless sensing solution enabled by discharge-induced displacement current. *Sci. Adv.* **7**, eabi6751 (2021).
39. Kuang, H. et al. Electric-field-resonance-based wireless triboelectric nanogenerators and sensors. *ACS Appl. Mater. Interfaces* **14**, 794–804 (2021).
40. Gu, H. et al. A battery-free wireless tactile sensor for multimodal force perception. *Adv. Funct. Mater.* **34**, 2410661 (2024).